iScience

CellPress
OPEN ACCESS

Article

Feature-preserving synthesis of termite-mimetic spinodal nest morphology

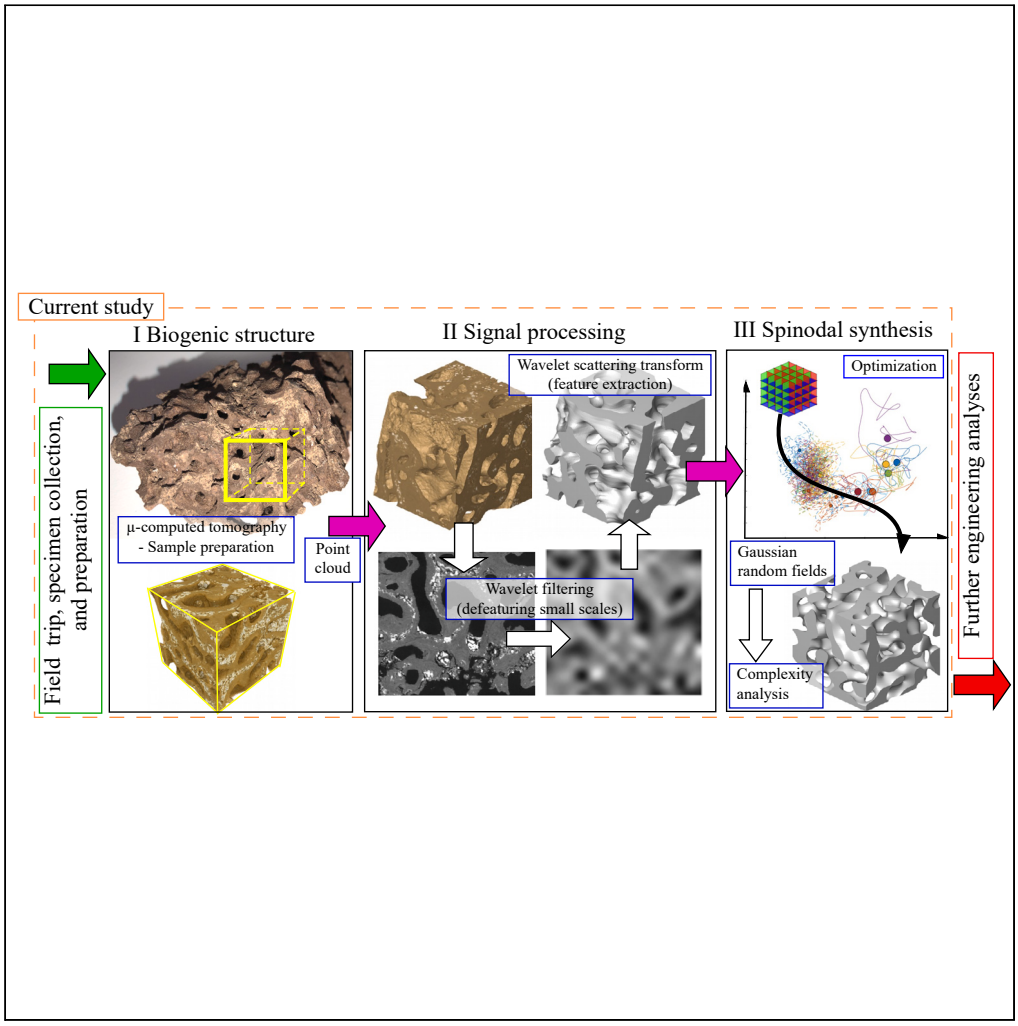

Sebastian Oberst, Richard Martin

sebastian.oberst@uts.edu.au

Highlights

Wavelet scattering transform's convolutional neural network is used for feature extraction

Gaussian random fields functions as surrogate to generate self-organized structures

Networked topology is not represented by complete graphs due to in-built functionality

Anisotropic biogenic geometry is shaped by the colony, which acts the global force

Oberst & Martin, iScience 27, 108674
January 19, 2024
https://doi.org/10.1016/j.isci.2023.108674

iScience

CellPress
OPEN ACCESS

Article

Feature-preserving synthesis of termite-mimetic spinodal nest morphology

Sebastian Oberst[1,2,3,*] and Richard Martin[1]

SUMMARY

Termite-built topology is complex due to group interactions and environmental feedback. Being interlinked with material characteristics and related to functionality, an accurate synthesis of termite mound topology has never been achieved. We scanned inner termite mound pieces via high-resolution micro-computed tomography. A wavelet scattering transform followed by optimization extracts features that are fed into a Gaussian Random Fields (GRFs) approach to synthesize termite-mimetic spinodal topology. Compared to natural structures the GRF topology is more regular. Irregularity is related to anisotropy, indicative of directionality caused by porous network connectivity of chambers and corridors. Since GRFs are related to diffusion, we assume that deterministic behavioral traits play a significant role in the development of these local differences. We pioneer a framework to reliably mimic termite mound spinodal features. Engineering termite-inspired structures will allow to inspect aspects of termite architectures and their behavior to manufacture novel material concepts with imprinted multi-functionality.

INTRODUCTION

Termites (Isoptera) form large colonies, archetypal of superorganisms, with amazing self-organizational features,[1–3] a form of extended phenotype.[4,5] Living underground and being blind, termites are considered soil engineers, famous for their complex nest constructions[6] and vibrational communication.[7] Their mounds i.e., the above ground nest, have attracted much attention.[3,8,9] Mound builders (mostly Termitidae) can be found in South America, Africa, and the whole Australasia[10,11] with mound heights ranging from only a few decimeters to several meters, varying shapes and materials, related to species-specific nest functions, modified through environmental conditions and interactions.[7,8] Inside the mound, termite-built organic structures are formed with specific features (morphology), and which serve multiple functions such as facilitating the nurturing of offspring, food storage, or to assist in the defense against intruders or protect against harsh environmental conditions.[7,8]

Certain geometrical features, and specialized materials used, together with the collective behavior of the swarm, guarantee the colony's survival.[12] Fractality (self-similarity) is ever-present within these biogenic structures.[9,12,13] Simplistically speaking and as conceptualized in Figure 1 A, the largest scale 'Scale 0' can be assigned to the mound followed by its functional topological layers. These layers are roughly classified as the outer shell, the periecie (peripheral box-work), and the endoecie (carton material) with, e.g., the breeding chambers or the royal cell.[7] In Figure 1B, 'Scale 1' is defined by a macroscopic clay design, corridors and chambers, curvatures, tortuosity ('bendedness'), surface roughness or surface arrangements[14–16] while 'Scale 2' (Figure 1C) shows the sheathing wall layers made of feces and saliva, perforation aka porosity (smallest volumetric elements) and granularity. 'Scale 3' (insert only) includes macroporous (> 50 μm to 75 μm up to several mm) openings, coined macroporosity in the following.[12] Finer scales, such as those related to mineralization, and composite elements or even the molecular structure, etc., are disregarded here, but could be described with additional scales 4 and 5.

At each scale of termite construction, different stigmergic principles can be assumed to be active in a living colony.[4,7,17,18] Stigmergy is here the spontaneous, indirect coordination between so-called agents, actions, or the environment.[19] In particular, scale 1 is assumed to embed important stigmergic cues, e.g., in curvatures, which are assumed to trigger collective building activities.[3,16] Recently, Facchini et al. (2020)[16] have investigated arboreal nests of Nasutitermes in a similar manner. By employing a Laplacian growth model, based on complex diffusion-type equations, they found striking similarities with respect to local curvatures.[16] Local curvatures are assumed to be important for transport processes and the efficient movement of the colony within the nest, and hence likely trigger stigmergy.[20–22] Recently, the argument of surface curvature was confirmed by studying *Coptotermes formosanus* building activities in artificial arenas, i.e., Petri dishes which indicated that curvature is the trigger for building, sensed via surface evaporation.[23]

Perna et al.[14] introduced computed tomography to visualize the architecture of *Cubitermes* sp. nests to study them using graph theory, while Himmi et al.[24] used computed tomography to study the tunnel system of *Incisitermes minor*, highlighting the termite nest as the morphological expression of the sum of termite behavioral patterns. While these studies consider only static states, Berville and Darrouzet[25]

[1]Centre for Audio, Acoustics and Vibration, University of Technology Sydney, Sydney, NSW 2007, Australia
[2]School of Engineering and IT, University of New South Wales, University of New South Wales, Canberra, ACT 2612, Australia
[3]Lead contact
*Correspondence: sebastian.oberst@uts.edu.au
https://doi.org/10.1016/j.isci.2023.108674

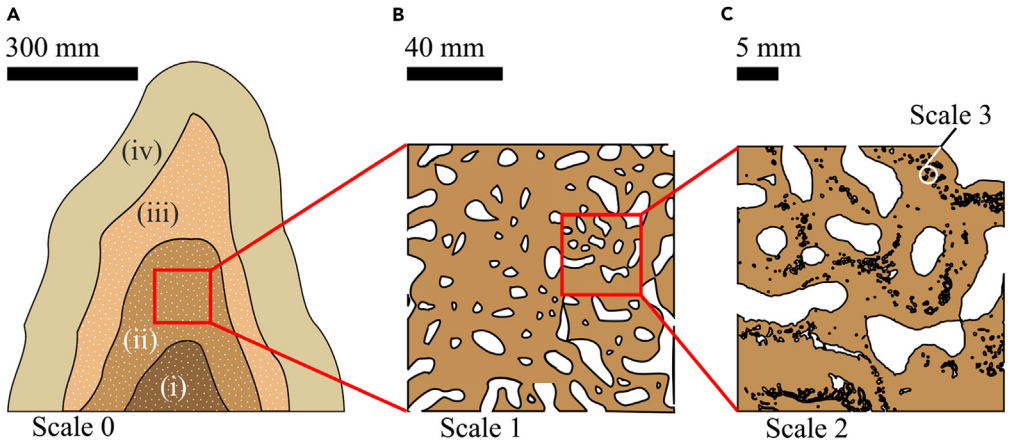

Figure 1. Scales of a termite mound

Different scales within one the above ground mound-nests (underground parts not displayed), with a more detailed view on the inner structure.
(A) 'Scale 0' the mound-nest parts, radially from the center (i) Nest, (ii) endoecie, (iii) paraecie, and (iv) hard shell according to.[7] The accurate modeling of (B) 'Scale 1' is subject to the research in this study; (C) 'Scale 3' as inclusions/scaffolding of 'Scale 2' has been reported in more detail in.[12]

also compared the nest construction in soil and wood of *Reticulitermes flavipes* and *Reticulitermes grassei* over time. However, as pointed out by Oberst et al.,[7] only medical computed tomography has been applied and no experimentally validated method of modeling the final construction state is known. Yet, due to the complexity of the internal structures, including tunnel constructions and wall designs, more accurate simulation, and for its physical models sophisticated additive manufacturing methods are needed.[3,9,26,27] With the advent of machine learning, neural networks and modern pattern recognition methods and with it the prediction of growth of spatial structures, a more accurate synthesis of termite topology seems achievable.[28,29]

Here, we collect termite nests and dissect them into pieces to scan them using high-resolution microcomputed tomography (μCT), similar to Oberst et al. (2021).[12] We use Gaussian random fields (GRFs)[30,31] as a computationally more efficient solution than Laplacian-based equations, and update these with features extracted using a wavelet scattering transform convolutional neural network.[32,33] A schematic diagram of this process is shown in Figure 2. We then synthesize more accurately internal structures of Scale 1 by preserving its features (Figure 1). Deviations to the original μCT scans are highlighted and discussed in the following in terms of termite biology by comparing the influence of scales and macroporosity,[12] as well as complexity measures.[34]

RESULTS

Termite mounds of two species, *Coptotermes lacteus*, a lower termite of Rhinotermitidae and *Nasutitermes exitiosus*, a higher termite of Termitidae were investigated. *C. lacteus* was collected during a field trip from the Tidbinbilla Nature Reserve (35°44′42″ S, 148°89′20″ E, Australian Capital Territory, Australia), while *N. exitiosus* was collected near the Australian Defence Force Academy in Canberra (35.1722° S

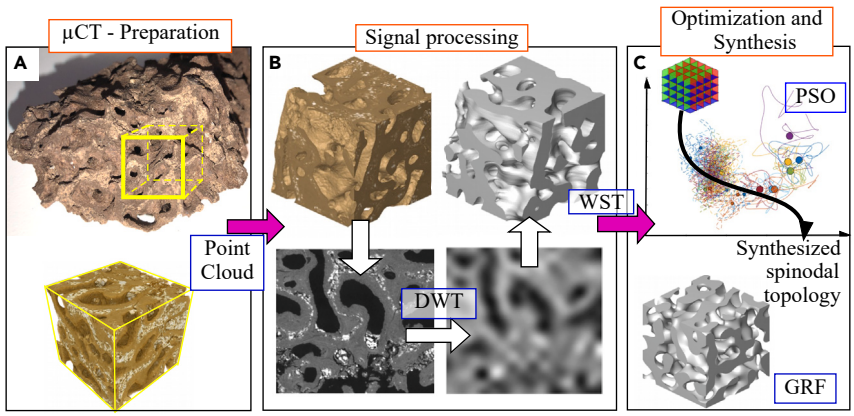

Figure 2. Conceptual diagram of GRF synthesized, spinodal termite structures

(A) μCT scans, (B) slice-wise de-featuring using the Discrete Wavelet Transform (DWT); (C) feature extraction using the Wavelet Scattering Transform (WST) on (e.g., 32) sub-volumes; and GRF particle swarm or surrogate optimization (PSO).

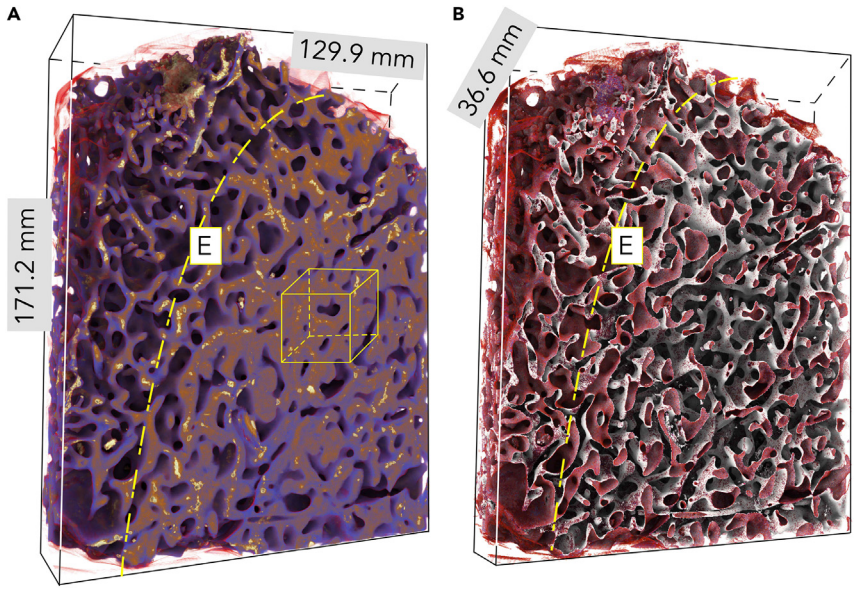

Figure 3. High-resolution micro-computed tomography (μCT)

μCT images of internal nest material of *C. lacteus* (A) scan with emphasis on only corridors (overview scan of *N. exitiosus* see Oberst et al. (2021)[12]); the yellow dash-dotted line [E] marks the boundary between box-work structure and endoecie[7,12] and indicates the volume of which three different cubes were cut out; (B) shows the corridor network removing all solid parts highlighting the complexity of how termites build.

149.0930° E). Nests were dissected, sorted, and vacuum-sealed (details see methods and materials as well as the STAR Methods section). Figure 3 exemplifies a large scan section of a high-resolution µCT image generated with Drishti.[35] Figure 3 A shows the µCT scan and its dimensions and the estimated transition (marked by [E]) to the inner endoecie.[12] Inscribed within the inner endoecie is a sample cube which will be used in the following to synthesize the spinodal structures. From the μCT scans point cloud data, three cubes of the *N. exitiosus* and one cube of the *C. lacteus* sample were generated for further deeper analysis (schematized in Figure 3). A cube edge length of 27 mm was chosen so that the cube was close to the largest possible cut-out of the μCT scan specimen excluding a surface of fracture resulting from the in-field sampling procedure. Figure 3B just shows the inner outermost layer around the tunnels, removing other inner wall material. The network structure and curvature of corridors play an important role in termite biogenics[3] and has been extensively studied as compared to the solid structural part.[12]

To filter out the finer details of the μCT scan (individual grains, smallest orifices), the image has been transformed into grayscale and a discrete wavelet transform (DWT) with symmetric wavelets is applied (see Oberst et al. (2014)[36] and STAR Methods). As a result of the DWT only the scale of tunnels, pillars, and walls is preserved. A surrogate optimization based on radial basis functions[37] is employed in sequence (several iterations) to extract optimal parameters of the wave vectors (frequency, directionality) of the GRF to model the filtered μCT scan best.[33] The cost function is the difference between the feature vectors of the wavelet scattering transform (WST) of the original structure and the GRFs.[32,33] The optimization was employed five times to investigate the stochastic spreading in the results (details see STAR Methods section). Figure 4 shows the results of the original data and the GRF optimized data. Differences are visible, yet both (the original and the synthesized structure show very high similarity. Table 1 shows the ranges of average optimized parameters of the wave vector bundle of the Gaussian random fields (GRFs) (frequency *f*, and values of anisotropy such as largest eigenvalue λ (to indicate the strength of the spread) of the covariance matrix of scattering space vectors and their rotation angles θ_z and θ_y), indicative for the direction, the final cost value, and estimates of porosity using Taud's method.[38]

In Table 1 the spread of the final cost values $costval_{final}$ is not very large, so it can be assumed that the solutions are near the optimal solution. The standard deviation for the frequency of the GRFs is low. λ, θ_z, and θ_y are extracted from the covariance matrix which describes mathematically the shape of a dataset.[40] Covariance, as measure of how much two variables (here directions) vary together relative to an output (here their synthesized volume) results in θ describing the directed deviation from the norm. It appears that θ_y of sample A is positive, which could be a matter of which part the nest was taken from or the particular shape of the original sample. Anisotropy of the GRFs as expressed by the largest eigenvalues λ, is not very prominent yet not close to unity. According to Kumar et al. (2020)[39] the structure exhibits cubic anisotropy (with symmetries), expressed through θ_z and θ_y. Porosity values (unitless ratios) are similar to the macroporosity reported in.[12,13]

To visualize the similarity of the optimized GRFs to the μCT scans, the dimensionality of the WST feature vectors of the GRFs and the filtered μCT scans is reduced using a principal component analysis (PCA). The first two components are plotted in Figure 5. The points for the GRFs and the filtered μCT scans are within two distinct, close-by clusters. The distance between points within one cluster is of the same magnitude than between points of the two clusters. The samples B and C are more similar to GRFs than the samples A and X. The

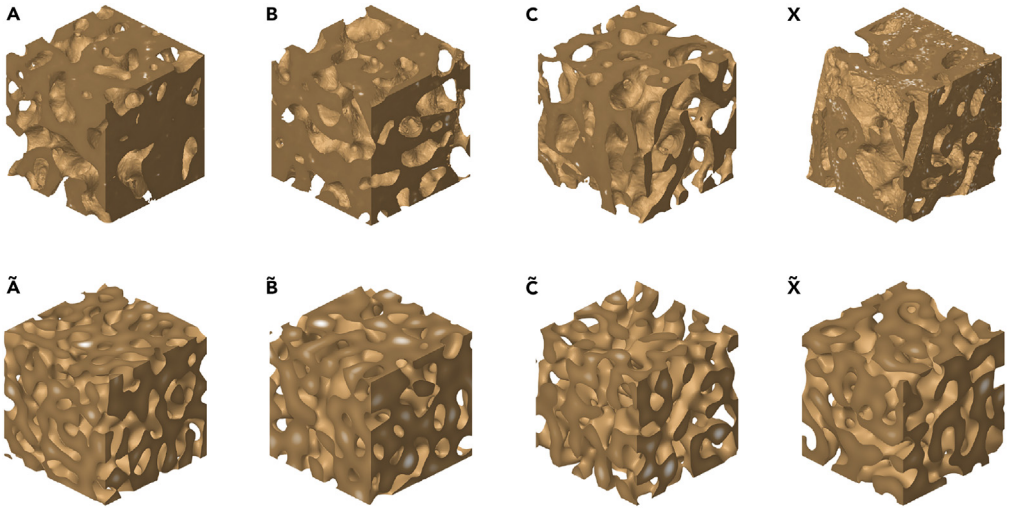

Figure 4. Raw data and GRF optimized structures

Unfiltered 3D samples A to C simply cut from the μCT scan of the nesting material of *C. lacteus* and X from *N. exitiosus* and examples for the corresponding GRFs using optimized parameters ($\tilde{A}$ to $\tilde{X}$).

optimization of the parameters of the GRF produces results which, while in feature space in close proximity to the original scan, can still be separated. While the large blocks show some similarity, the influence of scales is not captured.

Influence of scales

To investigate the influence of scales, sample C (*C. lacteus*) was chosen and eight sub-cubes are studied in more detail. Each of the sub-cubes C1 … C8 share one of the eight vertices of the large cube, respectively as shown in Figure 6A. For each of the sub-cubes the edge length *a* is varied from 1 mm to 26.4 mm in 1.016 mm steps. The same procedure is applied to both, the optimized and the synthesized GRFs. The features of the wavelet scattering transform of each subcube for μCT scans C1 to C8 are then compared to the features of the GRF-reproduced structures ($\tilde{C}1$ to $\tilde{C}8$) at each scale *a*. The dimensionality of this feature space is again reduced by employing a PCA.

The first two of these components are shown in Figure 6B and shows that the relative distance between the features of the μCT-Scan and the GRFs is small at small scales *a* between 1 mm and 5 mm (about the size of tunnels, see Figure 1). Submillimeter details (Scale 2) have been smoothed out before using the discrete wavelet filtering (Figure 2B). For an increased scale *a* for some of the vertices up to about 9 mm (which is about the diameter of chambers) the distances grow with feature values spreading over a greater range. This effect is attributed to the increase of different details of both the μCT-scan and the GRFs (rep and opt, Figure 6C).

The mean distance between each μCT-scan and GRF feature is plotted in Figure 6C. The GRFs are similar to that of the original μCT-scan for every vertex at the smaller scale (*a*). If the scale, i.e., the edge length of the sub-cube, is increased, the distance in the PCA increases and thus the similarity decreases. For some subcubes, especially C7 and C2, the similarity to a GRF decreases drastically with increasing scale. These sub-cubes cannot be represented by the rather regularly shaped GRFs. For very large scales, however, it can be observed that the distances seem to converge again to a single value. The sub-cubes must converge to the large (total) cube with increasing edge length. This value is lower than the maximum of the mean distances. Thus, local irregularities can be equalized on a larger scale by better fitting regions.

Table 1. Optimized parameters of the GRFs

Sample	A	B	C	X
f	2.85 ± 0.08	2.46 ± 0.03	2.45 ± 0.05	3.08 ± 0.1
λ	1.74 ± 0.64	1.42 ± 0.31	1.15 ± 0.63	1.41 ± 0.4
θ_z	$63 \pm 41\,^\circ$	$49 \pm 37\,^\circ$	$59 \pm 25\,^\circ$	$39 \pm 20\,^\circ$
θ_y	$17 \pm 29\,^\circ$	$-25 \pm 32\,^\circ$	$-49 \pm 28\,^\circ$	$-21 \pm 39\,^\circ$
$\text{costval}_{\text{final}}$	$5,601 \pm 63$	$4,425 \pm 18$	$4,142 \pm 21$	$4,831 \pm 35$
porosity	0.39	0.35	0.55	0.31

Optimized parameters of the GRFs and final cost values for five independent runs of the optimization and estimates for the porosity using Taud's method, while eigenvalues indicate anisotropy, θ-values indicate cubic symmetry according to Kumar et al. (2020),[39] both a clear indication of directionality of both, biogenic topology and GRF synthesized structure, and mismatch owing to reduced information on a different scale using the GRF approach.

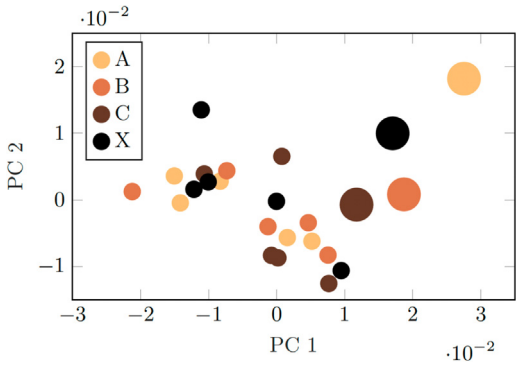

Figure 5. Reduced view on features of termite structures

Principal component analysis of the averaged WST features for each layer in *z*-direction for samples A to X. The large dots are the features of the termite-built structure (filtered μCT scan), the smaller dots are the results of the optimization.

This indicates that the optimization can effectively select the best set of parameters for a GRF to match the features of the μCT scan for a certain scale.

Comparison of porosity

Another common measure used to analyze porous structures is their surface-to-volume ratio[38] for which in the following only the interior surface areas, excluding their cutting surfaces, is considered. A large surface-to-volume ratio is relevant for termite to actively store moisture in their structures and to regulate humidity within the mound.[3,7] Figure 7 shows the ratio of the interior surface area to the total volume for both, the μCT scans (red, asymmetric distribution) and the GRF synthesized structures (family of Gaussians), as function of different porosity thresholds φ (vertical, dashed line shows actual value estimated with Taud's method[38]; other values are thresholds). The surface area to volume ratios for the GRFs are shaped parabolic with their maxima being proportional to wavelengths of the sinusoidal functions applied (cf. Table 1). The higher the frequency applied to the GRF the more interior surface area can be found within the total volume. The lower surface to volume ratio of the μCT scans indicates that volume and pores are not as evenly distributed as for the GRF. Larger volume sections of the solid phase within the μCT scan (lower frequency contents) reduce the interface surface area. The surface area-to-volume ratio of the GRF synthesized structure is only for sample X close to that of the termite topology.

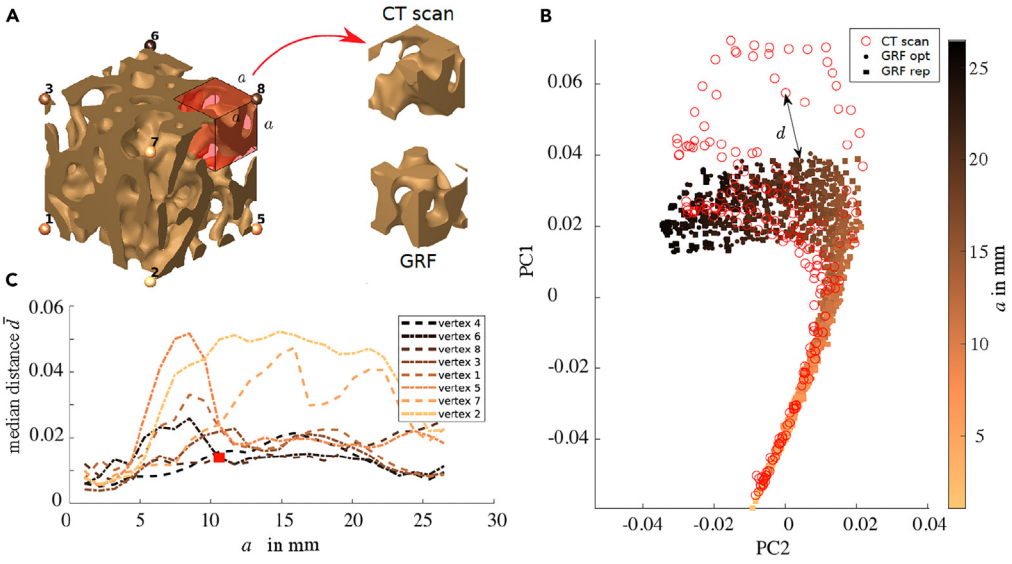

Figure 6. Analysis of scales using subcubes

Investigation of the scales of sample C (*C. lacteus*), Scale 3 (Figure 1C).

(A) Extraction of the sub-cube C8 with edge length *a* (after applying a smoothing filter).

(B) Principal component analysis of the wavelet scattering transform features of the μCT scan (red circles) and the optimized (opt) GRF (brown dots) and the synthesized (rep) GRFs (brown squares).

(C) Mean distances between the μCT scans and the GRFs. The red square marks the value for the sub-cube shown in (A).

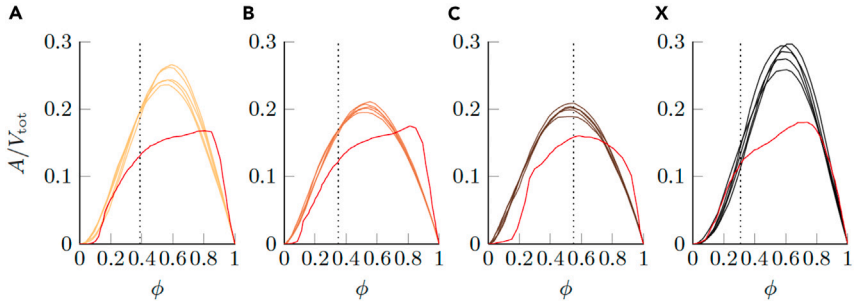

Figure 7. Porosity estimation

Surface area (A) to total volume (V_{tot}) ratio for filtered μCT scans (red, asymmetric distributions) and their respective GRFs V_{tot} (normal distribution curves). The vertical dashed lines show the estimated porosity (φ) of the μCT scans. (A–C) Relate to *C. lacteus* while (X) belongs to data of *N. exitiosus*.[12]

Measures of complexity

Next, the calculation of complexity measures is conducted. Classical measures based on the scanned geometry and the artificial (synthesized) structures are applied and compared to a recurrence plot analysis which uses the feature space trajectory (FST), formed by a PCA[41] of the feature vectors of the wavelet scattering transform for each layer in z-direction.

According to the permutation entropy H and the statistical complexity C shown in Table 2, the GRFs are about as complex as the filtered µCT scans while not being absolutely random (theoretically $C = 0$, $H \lim \infty$, i.e., no scaling[41,42]). Comparing the results among each other, only the correlation dimension D_2 shows consistently a slight difference with values for the GRF's being lower, indicating to be less volume filling. The dimension is finite and seems fractal (same behavior of a range of length scales[41,43] and of the same order as reported in Oberst et al. (2021).[12] Together with values of the entropy and the statistical complexity this implies that both structures resemble each other (without being necessarily qualitatively equivalent).

The FST of the μCT scans has a long tail, corresponding to a section of the sample dissimilar to the rest. The FST of the GRF however is more compact without long tails, indicating a regularly shaped, feature-poor structure, as also confirmed by the respective RPs (Figure 14). For $z > 100$ there are no recurrences for the μCT scan, while for the GRF there are no isolated parts in the RP. The RP for the μCT scan resembles a transient dynamical system, whereas the RP for the GRF resembles a nonlinear system.[44] The period of the pattern in the recurrence plot of the GRF corresponds to the frequency of its wave field, which can be generally distorted by its anisotropy.

Table 2. Estimation of complexity measures

	μCT scan - original data			
	A	B	C	X
D_2	2.706	2.733	2.561	2.752
H	0.7496	0.7576	0.7572	0.7658
C	0.3873	0.3848	0.3883	0.3815
RR	0.06	0.04	0.08	0.09
L_{MAX}	10	10	20	14
ENT	1.83	1.68	2.18	1.94
	Gaussian Random Fields (GRF) - synthesized data			
	$\tilde{A}$	$\tilde{B}$	$\tilde{C}$	$\tilde{X}$
D_2	2.615	2.677	2.479	2.687
H	0.770	0.757	0.758	0.775
C	0.391	0.403	0.404	0.383
RR	0.09	0.10	0.10	0.15
L_{MAX}	14 ± 5	19 ± 3	16 ± 5	16 ± 5
ENT	1.91 ± 0.38	1.94 ± 0.30	1.98 ± 0.15	1.92 ± 0.18

Estimates for the correlation dimension D_2, the permutation entropy H and the statistical complexity C and Recurrence Quantification Analysis (RQA) measures for various samples and their respective GRFs. For the GRFs the standard deviation for a set of five samples is provided to quantify the spread of values for different optimizations.

The results of a Recurrence Quantification Analysis (RQA) and that of an invariant extraction (correlation dimension D_2, permutation entropy H, and statistical complexity C are shown in Table 2. The GRFs, due to their more compact FST, have a higher recurrence rate RR than those of the μCT scans, see Figure 14. The maximal line length $LMAX$ is generally higher for the GRFs than for the μCT scans, indicating a more periodic behavior, however the spread of values is quite large. The Shannon entropy of the probability distribution of diagonal line lengths $ENTR$ between GRFs and the μCT scans is quite similar for both cases A, C, and X but lower in case B for the μCT scans.

DISCUSSION

Termite structures have been studied extensively in the past, with main focus on their networked tunnel system, building activities or nest self-ventilation and acclimatization characteristics.[3,9,15] Yet, modeling of whole mounds or even parts of them has rarely been attempted, and certainly not with a great level of detail. Here, we combine various methods (feature extraction, signal processing, optimization, GRFs) into an analysis framework and experimental data of collected termite mound segments for the synthesis of termite-mimetic spinodal structures.[45] Examples of using GRF on other information e.g., to study regular lattices, or noise can be found in literature.[39,46]

Scale 1 (see Figure 1), related to the corridors and the chambers, has attracted some recent interest[16,20] in that it was assumed that collective termite building behaviors are triggered by geometrical features rather than a diffusion pheromone.[7,16,20,47] While there is more knowledge available related to termites as soil engineers, and their material used and associated macroscopic stability,[48–52] only very recent novel high-resolution μCT imaging data have revealed multi-scale structural details of biogenic topology and their complex micro-composite character.[12]

By applying the same μCT technology as used in Oberst et al. (2021),[12] we focused here on the local scale of the nest, corresponding to corridors and chambers within the endoecie of the two species *C. lacteus* and *N. exitiosus*. By doing so, we were able to better inform effective mathematical models to synthesize localized macroscopic nest features for the first time by preserving implicitly natural features.[7] Most Isoptera comply with certain requirements to their buildings, so-called templates.[3] Further, and that is true for most termites, temperature and humidity of the mound must be regulated, metabolic gasses must be exchanged, and termite traffic has to be coordinated efficiently. Additionally, the nest serves as a fortress against predators, a cradle to new generations of termites, and a pantry for the forage.[8] Hence, the mound and the structure at certain locations within the mound must serve different requirements which are species-specific.[7] Functions compete on a local scale; thus, termites need to optimize their efforts during foraging and use of materials during building spatially and temporally.[48,49]

Engineering synthesis of spinodal geometries and differences to biogenic structures

We employed the wavelet scattering transform (WST)[36] to extract features and to optimize the parameters of GRFs as temporal-spatial stochastic process.[33,53] The extracted WST features are in qualitative agreement with those of natural porous structures, proving the suitability of the method chosen for the selected scale. The approach is computationally efficient and does not require a sophisticated feature selection process.

However, some differences persist. For topology designed by Isoptera, the diameter of the tunnels and cavities is influenced by the need of gas exchange and to accommodate efficient termite movements/colony traffic, or storage of food and brood.[8,26] The walls need to have a certain thickness to support the gravitational load and external forces on the structure and to store moisture. GRFs have shown to be useful to model the macroporous structure on the scale below 5 mm however, due to being generated by superposing sinusoidal waves of a single frequency and due to local design objective changes within the mound, larger structures are more difficult to model accurately as indicted by both the two-point auto-correlation function (Methods and materials) and the surface area-to-volume ratio (Figure 7).

Since GRFs are solutions to diffusion processes, the local shape of the internal structure of the mound is formed by those. During the building of the nest, the movement of individual boluses,[12,54] i.e., termite soil pellets (termite bricks) of up to 1.2 mm in diameter ball-shaped building units formed by soil particles, feces and saliva, is a dynamic process resulting in smooth structures. Smooth inner tunnel and chamber walls[12] facilitate air flow and movement of the colony within in the mound. Further, smooth geometries reduce the notch effect,[55] which implies that stresses are less concentrated, which induces larger resistance, and higher mechanical stability.[48,50] Whether local smoothing activities are likely to happen continuously, in a converging sense, through termite stigmergic actions within the mound, or while progressing tunnel construction during building, remains to be studied.[26,27]

Anisotropy through directionality

Other differences are related to the connectivity of parts within the nest. Perna et al. (2008)[15] studied the corridor network in nests of *Cubitermes*, where bulgy chambers are connected by thin tunnels while Hu et al. (2023)[56] made use of termite morphology to design a bionic heat sink, which is strongly dependent on high connectivity. Here we analyze the structures of *C. lacteus* and *N. exitiosus*, where the cavities cannot be grouped into chambers and tunnels. Instead the network consists of highly interconnected pores of various widths and lengths, similar to that found in pore network models of reactive transport applications.[57] Similarly, we find that the natural termite structures are more complex as shown by their difference in recurrence rate RR and higher correlation dimension D_2 (Table 2). While the optimization parameters provided excellent results to engineer artificial termite nest endoecie, their eigenvalues λ and the rotation angles θ_z and θ_y indicate anisotropy (Table 1). While anisotropy in self-organized systems usually relies on global body forces, such as gravity or magnetic fields,[58] we assume that termites as a collective of many individual insects can make use of those forces to shape their structures in a certain way. That this is the case is indicated

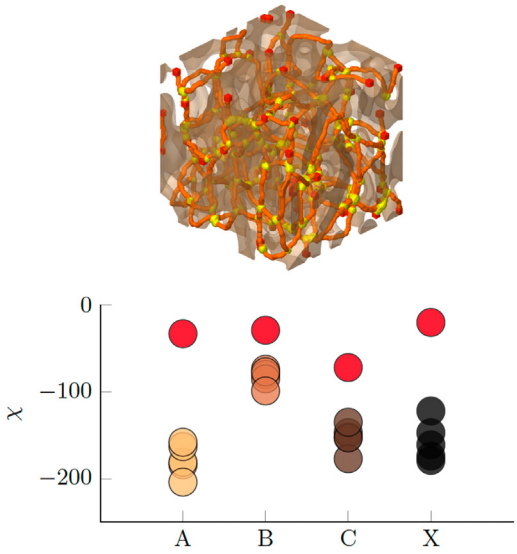

Figure 8. Network analysis

Top: Network of μCT sample C with branching points (yellow) and endpoints (red). Bottom: Euler characteristics for the μCT scans (red dots) and their respective optimized GRFs.

by the mound structure which is revealing in those termite species studied concentrically differing topological layers, with the nest as the mounds' center point. The shaping and loss of degrees of freedom (*dissolvance*, Testa et al.[59]) likely originates from the metabolism, the heat generated, changing gas concentrations, humidity variations and mass flow, which generates a quasi-forcefield in the center of the mound nest.[7] Differences in the sign of Table 1, 'θ' could be related to different orientations of the originally scanned sample. Systematically studying the development of the co-variance using more samples and moving across different nests would provide a deeper understanding of the differences observed here.

Higher complexity, and stronger irregularity are evidenced through the two-point autocorrelation function (see STAR Methods). To investigate whether the connectivity of the pore network contributes to differences found we used the Euler characteristic χ.[60] Figure 8 shows the Euler characteristic for all samples, with lower χ being indicative for higher pore connectivity. Sample C shows the highest connectivity and highest porosity of all μCT scans. However, the Euler characteristics of all GRFs are significantly lower than those for the respective μCT scans indicating a higher connectivity, especially in samples A and X. In geology and here especially percolation theory, the relation between anisotropy and networks (fracture, porosity) as expressed through graphs is well understood.[61,62] Highly connected graphs appear isotropic while directional flow networks and incomplete graphs cause high anisotropy and reduced pore network connectivity.[61,63] Termites collectively shape the structure of tunnels and their connectivity with time, forming pillars and layers,[3] and on different scale (having smooth surfaces or certain i.e., optimal surface properties where fast walking is required). While Laplacian processes, including GRF, produce matching curvatures on a local scale,[16] their macroscopic geometrical pattern rather indicate deviations to real-life structures of termites. Rather than simply following random processes, paths and corridor directionality can be assumed to be shaped by their biological functions.[7] One important function is the ventilation of the mound[9] and with it the temperature management.

One indication of relatedness to biological functions and local anisotropy including ventilation (while qualitatively different, known from localized defects, such as resistance anisotropy in otherwise theoretically isotropic structures[64,65]) is shown in Figure 6. The similarity at low scales, i.e., tunnel/corridor is high, however, when it comes to larger sizes, the average difference between natural biogenic and synthesized spinodal structures is stronger. This difference becomes pronounced at mid-scales due to the nonexistence of clear chambers in the GRF optimized structures. Tunnels move into chambers produce a sudden change in the characteristic dimension, a transition less often observed in GRS; at larger scales, we do not know the exact reason for this deviation, but tunnels and chambers could a certain direction and shape rather than being random, which need to be further explored. Here, evenly distributed periodic structures, i.e., cavities and tunnels, would account for an isotropic material, which is produced if the GRF was not updated as shown for other structures in Kumar et al. (2020).[39]

In Perna et al. (2008)[15] in a nest of *Cubitermes* spp. low connectivity was observed, which is also the case here for nests of (*N. exitiosus* and *C. lacteus*). Lower connectivity relates a statistically larger path length between two arbitrary points and likely has its root cause in an advanced defense strategy against intruders. The GRF-synthesized structures, however, are much more regular and more interconnected than their biogenic counterpart despite showing very similar porosity. Termites balance the need of ventilation and managing their temperature with that of traffic and defense against predators, structural toughness, and material requirements.[12,48] Hu et al. (2023)[56] have developed a bionic heat sink based on termite-inspired, self-organized morphology, also using a Gaussian surrogate model. Results showed for a specific hot spot temperature a pressure drop of 51%, while reducing temperature variance by 60% by only increasing the solid volume by 3% which is achieved for high connectivity.[56] A lower connectivity, however, is representative of an incomplete undirected graph, which is often found in

termite mound networks. This is similar to anisotropy being a measure for directionality, and is therefore represents a measure of *specialized functionality* as opposed to mere connectivity, embedding this way spatial information[66] within the termite mound. Yet, how exactly connectivity and exact termite structures are related to heat and mass transfer for ideal ventilation conditions within the mound remains to be studied.

Due to the limitations and simplifications of the GRF approach, the parameters controlling the anisotropy of the GRFs show slight but distinguishing differences (see Table 1). The samples for this study are isotropic at a larger scale, but they have some important local irregularities, which can only be estimated to a certain degree with the current GRF-based approach and which show up in eigenvalues (Table 1) being greater than unity. This is to some degree expected since in a termite mound, the topology must be anisotropic, owing of the directionality of natural forces, such as gravity, solar irradiation, or convective air flows but also the internally shifting of biomass (termites). Termites design local functional morphology, like tunable anisotropic material behavior.[39] Different geometries on different scales such as the comparison of the endoecie to the carton material in the nesting section[67] resemble a spatial transition from cubic to lamellar anisotropy.[39]

For the dimensions as explored in this study (27 mm) the samples and sub-samples already comply to the aforementioned conditions to a different extent, resulting in complex, irregular structures which also include asymmetries which are not covered by the GRF approach. Asymmetrical dynamics have also been illustrated in the recurrence plots, which resemble transient, nonlinear processes. Differences in the recurrence plot quantification and plots are assigned to the smoothing (loss of information on a smaller scale) and the synthesis of the structure as well. To measure directly asymmetry, it is in principle possible to calculate and measure e.g. Willis coupling parameters relative to an impinging acoustic wave.[68] This is important as termite structures respond as a system to physical input quantities (acoustic pressure, humidity and airflow, vibration, stress, and strain) as termite mounds serve multiple functions.[7] Function might be consistent with certain parts of the nest and the behavior therein, hence the structure might be subdivided and is likely to be interchangeable to a certain degree, depending on the nest's hierarchical topology, or developmental stage. These functions and in a wider sense termite behavior, might therefore be molded in clay (as suggested by Perna and Theraulaz (2017)[3]), yet detailed studies on how stigmergy, building activities, and phenomenological designs are correlated and may lead to anisotropic topology have never been reported to-date.

Observed differences for species

Between the species *Coptotermes lacteus* and *Nasutitermes exitiosus* visible differences in their outer endoecie are apparent (Figure 9), see also data in.[45] For *C. lacteus* no strong inner scaffolding was observed, rather laminar structures[12] with high-density pillars/elongated cylindrical beams accompanied with a hard outer shell (absent in *N. exitiosus*).[7,69] Building the termite nest costs energy, and incorporating a thermal isolation layer which is also able to sustain greater loads stability by designing a scaffolding might turn out to be more energy efficient on the colony level.[48] As indicated by Korb (2010)[8] mound shape and composition of layers especially the outer layers play an important role in acclimatization of the nest, either based on ventilation through ducts or through diffusive gas exchange via thin, brittle outer sheeting layers as in case of *N. exitiosus*.[7] Yet both, thermal properties as well as stability aspects of termite-built biogenic topology[49,50,54] require to be systematically explored across Isoptera. The distribution of *C. lacteus* and *N. exitiosus* overlaps but the latter species prefers warmer climate which renders a thick outer shell less important.

The tunability of the internal material composition may follow different demands of colony development influenced by season, state of health, or other longer-term scenarios. Stigmergic cues (i.e., spatial embedding of information) may therefore be related to the geometry rather than to a diffusion pheromone,[3] and instead of having a single cue, termites build and design their nest through cascading, independent factors.[7,12] Considering the small value of the threshold criterion, absolute values reported here are small, yet show an important, but rarely detected and never reported difference between geometries which resemble each other closely. With a more advanced model, which has more degrees of freedom and can be tuned locally, larger samples of a termite topology could be synthesized and then modeled more accurately. Local tuning could be achieved by controlled fading between GRFs with different properties, resulting in a reconstruction technique similar to representing objects via 3D wavelets with multiple resolutions.[32,70,71] Kumar et al. created 3D hierarchical nano-lattices with individual beams of multiple self-similar unit cells spanning length scales over four orders of magnitude in fractal-like geometries such that their generated GRFs matched the anisotropic properties and geometry of a bone sample.[39] Using the sequential approach suggested here combined with[39] will shed light on features and their functions, and will eventually lead to the generation of a high-fidelity digital model of a termite nest. An accurate model with predictive capabilities needs to embody the same trade-off principles, which are followed by termites, while building and maintaining the topology, leading to Pareto optimal solutions – something which needs to be understood in context with termite evolution, and behavioral ecology. However, the optimization should take place on more scales of the termite mound, from the very large scale of the overall mound shape, over the larger network of tunnels and support structure, to the local pores and the composite wall material.

Outlook

To better understand stability and strength as well as air flow, cooling etc,[9] similitudes using different 3D printed samples of different materials could be estimated using for instance compression tests, and larger computer models of termite feature preserving characteristics should be produced to generate an phylogenetic tree and link it to termite nest topology and its multi-physical properties. The inner topology's importance on air-conditioning and self-ventilation[9] through evaporative cooling requires exact geometry which is possible to achieve following the design process described in this paper. In turn, the influence of different environmental templates (airflow, mechanical properties, etc.) on the inner local macroporous termite structure can now also be further investigated.[3] A computational framework of this study should be adapted to accommodate any new model for macro-porous termite structures and check the

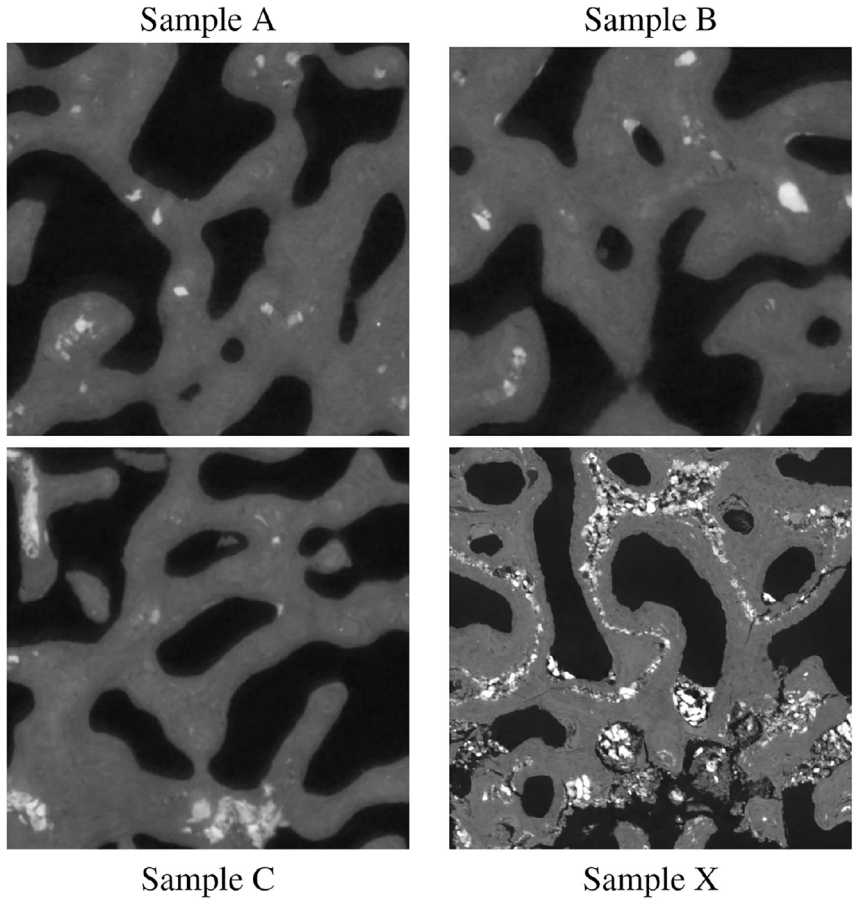

Figure 9. μCT scan examples

Differences in terms of inclusions for example slices of sample cubes (A–C) and X can be observed (Scale 2), while the macroporous structure looks similar by judgment of the bare eye (Scale 1).

suitability as measured by the dynamical and morphological measures. In the long term, more scans of different samples of mounds of various species are needed to study how the termites adapt their structures to environmental conditions, sources of food, or predatory threats. Similar to Ocko et al.[72] who employed the advection-diffusion equation, a deterministic approach based on partial differential equations could be employed to investigate the morphogenesis on different scales, by considering e.g., the inner scales which have shown to be structured like an inverse Brazil nut effect.[12] Such a deterministic model could potentially reflect also the dynamics of self-organization and be compared to the final result of the GRF. Understanding better the function of the mound and its scale as well and its strong connectivity to the colony is an essential step in fully understanding termites as superorganism and their nest as their extended phenotype.[67]

Methods and materials

Collection of specimens and μCT scans

Collection of termite nest material. For this study a termite mound of the species *C. lacteus* was collected from within Tidbinbilla Nature Reserve (35.456°S, 148.927°E); we also dissected as well as a mound of the species *N. exitiosus*, near the Australian Defence Force Academy in Canberra (35.30°S, 149.17°E, Australia), cf.[12]

Parts of the nesting material were scanned using a high-resolution μCT which provided submillimeter accuracy.[12] Sample μCT images of the of the two species are depicted in the composite Figure 9. The *C. lacteus* mound was about 900 mm height and had a diameter of about 1,000 mm, cf. methods and materials, Figure 10. The mound of *Na. exitiosus* had a height of about 300 mm and a diameter of ca 650 mm, cf. Oberst et al. (2021).[12] For both mounds, the outer soil capping was removed, and the different parts of the mound were broken into large fragments which would fit into zipper bags and placed into a large portable cooler (70L, Esky rugged), cf. Figures 9B and C. The samples were transported to University of New South Wales, Canberra, where they were further dissected. We cut two samples of the outer endoecie from the two mounds, one was found after a peripheral box-work (periecie) in case of *C. lacteus*,[7] while for *N. exitiosus* the specimen taken was

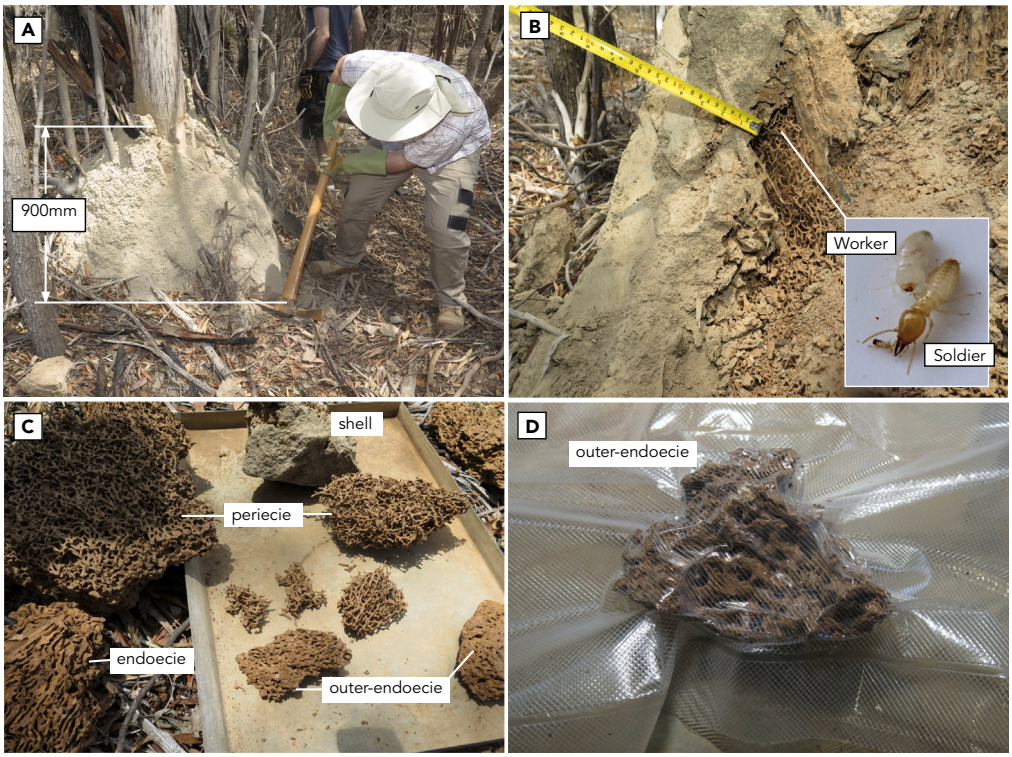

Figure 10. Termite structure specimen collection

(A) Termite mound of *C. lacteus*; (B) opened mound and thick outer shell and termite worker and solder as inset; (C) different mound segments as identified; and (D) vacuum-sealed piece of outer endoecie, representative for Scale 1 (Figure 1) as analyzed in this study.

found about 100 mm below the outer soil capping. Both specimens cut via a spatula into sizes of about 80 mm × 70 mm × 95 mm and sealed off in vacuum bags (Ambiano, multifunction sealer) to reduce humidity/moisture losses and to avoid crack development/propagation through desiccation (Figure 10D).

Computed tomography of termite nest structures

At the Australian National University's (ANU) μCT facility (CTLab) we applied high resolution X-ray helical μCT to analyze the geometry of the termite-built structures directly within the vacuum-sealed bags, cf. Oberst et al. (2021).[12] For this purpose, a transmission-type X-ray source, with beam voltage and current of 80 kV and 110 μA was used, respectively. The samples were scanned and converted into 2D image stacks using ANU's Multi-modal Australian ScienceS Imaging and Visualization Environment (MASSIVE) imaging and visualization cluster. Tomography renderings and porosity percentages were produced using ANU's supercomputing facility to run ANU's Medial Axis and Network Generation software (Mango)[73,74] and Drishti volume rendering software.[12,35] The scanned dataset was first uploaded using "Drishti Import", then further (in "Drishti main") modified in domain and using FRFs for different densities using 8-bit resolution before being saved as project and visualized using the 16-bit option.

Methods for synthesis process and analysis

Wavelet Scattering Transform. The image slices of the scanned structure were then de-featured using a 3D DWT (decomposition and synthesis) using sym32 wavelets, before the *wavelet scattering transform* was applied (see Figure 2B).Features are then extracted using the Wavelet Scattering Transform (WST) by Bruna and Mallat.[75] This method is based on a Convolutional Neural Network using wavelets[32] as predefined filters, so no training is needed. The working principle of the wavelet scattering transform in 1D space (ξ) with construction filters φ, λ_1, and λ_2[76] is shown in Figure 11. Here, $\boldsymbol{I}_1$, $\boldsymbol{I}_2$, and $\boldsymbol{I}_3$ represent three locally invariant descriptors extracted from the scattering coefficients S_0x, S_1x, and S_2x for translation, average signal amplitude, and transient phenomena.[76]

Here, three layers (two wavelet filter banks) are used with x scales and y rotations each. The three layers compute zeroth, first and second order features (scattering coefficients) of 2D slices of the cubic samples (coefficients of invariant features $\boldsymbol{I}_0$, $\boldsymbol{I}_1$ and $\boldsymbol{I}_2$ in Figure 11). To capture the three-dimensional nature of the samples, n slices in the three Cartesian coordinates are taken and its features are calculated. Results on benchmark systems, such as lamellar, columnar, and cubic examples[39] show that the energy of the third-order scattering coefficients is likely negligible (less than 1%).

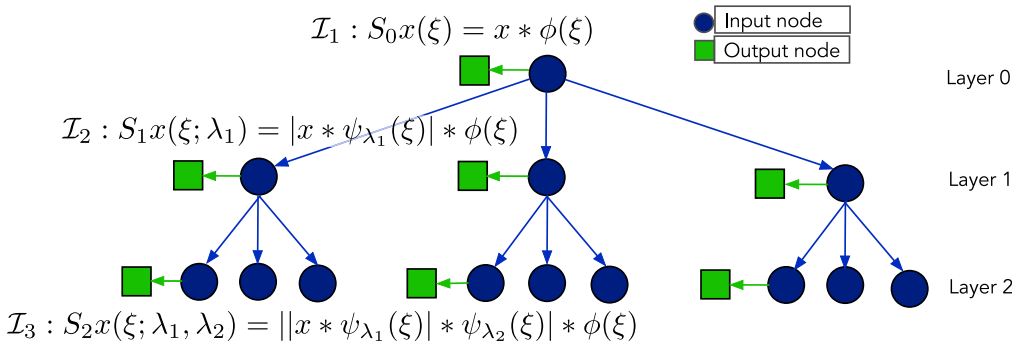

Figure 11. Wavelet scattering transform

Schematic of the extraction of scalogram coefficients using the wavelet scattering transform (adopted from[76]). The schematic shows three layers (and two non-zero layers), with circles representing input data and squares output data.

Topology synthesis. GRFs have been used to model nanoporous gold, biogenic structures such as bones,[39,77] and to model higher-dimensional complexes, including geostatistical and areal (lattice) data, complex, optimized designs or also term structure of interest rates.[30,31]

GRFs can be in principle of dimension 1 or also higher dimensional. A one-dimensional GRF is called a Gaussian process[40] and is following the Gaussian distribution (forming the bell-shaped curve) over time. A Gaussian process is a stochastic system changing over time. The Gaussian probability density function here is the underlying property and provided with

$$p(\mathbf{x}) = \frac{1}{\sqrt{(2\pi^d|\Sigma|}} exp\left(-\frac{1}{2}(\mathbf{x}-\mu)^T\Sigma^{-1}(\mathbf{x}-\mu)\right) \quad \text{(Equation 1)}$$

with $\mathbf{x}$ being the vector of input variables, μ being the mean with $\mu = \frac{1/N}{\sum_i} x_i$ and $det(\Sigma) = |\Sigma|$ being the determinant of the input variables covariant matrix. Having a sampling of a certain quantity, e.g., position d (as the case for Brownian motion, Random walk processes[40]) one can extract a random process at time step t_i such that $d(t) = d(t+\delta t) - \delta d$, where δd is a random distance from the previous position drawn from a population of normally distributed samples (e.g., here with a stationary mean, hence $\approx \mathcal{N}(0,\delta t)$); and $d(t)$ is the changing position over time. In theory, and if generalized, GRFs are infinite dimensional Gaussian processes over distributions of functions $f(\mathbf{x})$ whose distribution is defined over a mean function (or *mean* in the discrete case) and a positive definite covariance function. The covariance function becomes in practical (finite dimensional measurements) the *covariance matrix* and the random field would be approximated through multivariate Gaussian (marginal) or joint normal distribution[40,48]). In the following we are looking at wave vectors $\mathbf{x}$ instead of distances d and indicate their directions and the phase angles with $\mathbf{n_i}$ and φ_i as shown in the following,[39]

$$\mathbf{f}(\mathbf{x}) = \sqrt{\frac{2}{N}}\sum_{i=1}^{N}\cos(\beta\mathbf{n}_i\mathbf{x}\cdot\mathbf{x}+\varphi_i). \quad \text{(Equation 2)}$$

Here, $\beta\mathbf{n}_i = q_i$ with $\beta > 0$ representing a constant wavenumber and $\mathbf{n_i} \approx \mathcal{U}(S^2), \varphi_i \approx \mathcal{U}([0,2\pi[)$ with S^2 describing the unit sphere in $\mathbb{R}^3$ (details see[39,78]). Equation 2 describes a Fourier solution of three dimensional diffusion processes e.g., the non-anomalous heat diffusion equation[79]; the Gray-Scott reaction diffusion (GSM) equation[80]). We use random initial conditions, and therefore describe a structure through super-positioning sinusoidal composition modulations with random amplitude, orientation, and phase,[81] but in space such that

$$\mathbf{f}(\mathbf{x}) = \mathbf{f}(\mathbf{x}+\delta\mathbf{x}) - \delta\mathbf{f}. \quad \text{(Equation 3)}$$

The formation of the overall structure is therefore intrinsically more holistic, and different compared to that of e.g., engineered metamaterials, with an (often unimodal, highly functional) unit cell (meta-atom), which is explicitly architected after deterministic principles.[82] Anisotropy as observed in GRF can be accounted for by manipulating the covariance matrix Σ of the Gaussian distribution (Equation 1) of the three-dimensional wave vectors. The covariance matrix can be constructed using the eigendecomposition, i.e., factorization of a diagonal matrix into canonical (or normal/standard) form[40]

$$\mathbf{\Sigma} = \mathbf{U}_{rot}\cdot\mathbf{\Lambda}\cdot\mathbf{U}_{rot}^{-1} \quad \text{(Equation 4)}$$

where $\mathbf{U}_{rot}$ is the matrix expressing the rotation of the principal axis of the multivariate Gaussian distribution and $\mathbf{\Lambda}$ is the diagonal matrix (with eigenvalues λ_i as diagonal elements) defining the stretching or compression along the principal axis. The rotation angles are θ_z and θ_y for rotations around the y- and z axis respectively (assuming ellipsoids in 3D; or iso-density loci plotted in $x-y$-plane for bivariate distributions.[40]

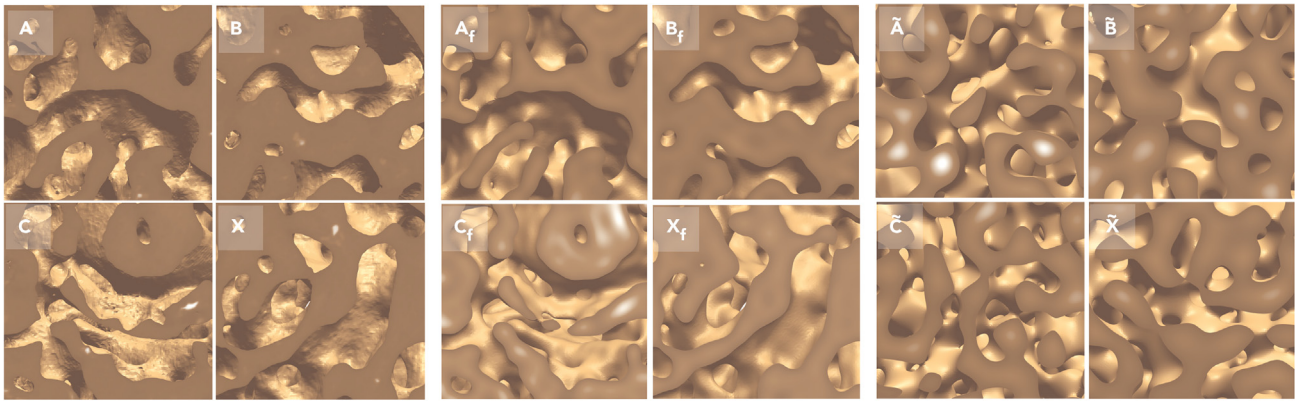

Figure 12. Examples 2D slices taken from subcubes

Two-dimensional slices of cubes of 29.6 mm edge length. A-X: original μCT scan, A_f-X_f defeatured μCT scan, and $\tilde{A}$) - $\tilde{X}$ synthesized structure using GRF. While the original scan shows many more small-scale features, the, the defeatured structures are smoother, yet more irregular than the GRF synthesized topology.

The rotation matrix is orthogonal, thus $\mathbf{U}_{\text{rot}}^{-1} = \mathbf{U}_{\text{rot}}^{T}$. The resulting wave vectors are normalized, such that they describe points on a sphere, of which the radius corresponds to the frequency of the field. For a strongly anisotropic GRF the vectors point in a certain direction, for an isotropic field they are distributed evenly over the whole sphere and the covariance matrix is the unity matrix.

To tune the parameters of the GRFs a surrogate optimizer based on swarm optimization (Figure 2C) is employed[37] with the objective to minimize the difference between the feature vectors of the wavelet scattering transform and the GRFs. Later, the samples and the GRFs are compared using a PCA and measures from dynamical systems theory, as well as geometry-based features.

A result of this optimization procedure is shown in Figure 12, comparing the original scan (A-X), the DWT filtered scans (A_f - X_f), and the GRF synthesized structure ($\tilde{A}$ - $\tilde{X}$).

Differences in the two-dimensional view become more obvious than in three dimensions (compare with Figure 4). After filtering and removing some small-scale features (A-X), while locally similar, the cavities within the GRF synthesized structures ($\tilde{A}$ - $\tilde{X}$) appear to be more evenly distributed. They also seem to have more connections resulting in less evident corridors. Corridors are wide and reduce to bottlenecks (of about 1 mm diameter) at some locations, rather than having pronounced chambers, which is different from the GRF synthesized structure. However, the non-perforated corridors in the natural structures account for some distinct directionality. The GRF synthesized structures also show more acute angles and sometimes sharper corners which are absent in the natural structures. Otherwise, no clear differences between samples A-C and X can be observed, which might be attributed to the scale.

Two-point autocorrelation function. To analyze self-similarity and repetitions within a structure, the spatial distance between variables can be estimated using the correlation (or two-point autocorrelation) function.[77] The distance between the first local minimum and the first local maximum represents the characteristic length within the structures, representative here for the width of tunnels and wall thickness.

The two-point autocorrelation function Γ, normalized with φ, can be expressed as the ensemble average[77]

$$\Gamma^{\text{norm}}(r) = \frac{\langle \boldsymbol{\mathcal{I}}(\mathbf{x}_i)\boldsymbol{\mathcal{I}}(\mathbf{x}_j)\rangle - \varphi^2}{\varphi - \varphi^2} \qquad \text{(Equation 5)}$$

where $\boldsymbol{\mathcal{I}}(\mathbf{x})$ is 1, if $\mathbf{x}$ corresponds to the solid phase, and otherwise it is zero. Γ is calculated for sets of points with different distances $r_{i,j} = |\mathbf{x}_i - \mathbf{x}_j|$, i.e., it is the ensemble average over the surface of a sphere around $\mathbf{x}_i$ for all points of the domain. To save computational effort, 1000 points of the solid phase are chosen at random for $\mathbf{x}_i$. One can see the resemblance to the correlation integral (6), where the ensemble average over all solid points *inside* a sphere around $\mathbf{x}_i$ is calculated.

Every two-point auto-correlation function, Figure 13) of the μCT scans show local minima and maxima, which are yet less prominent compared to those of the GRF synthesized structures, due to higher irregularity ($\propto$ complexity) found in termite-built topology. The distance between the first local minimum and the first local maximum represents the characteristic length within the structures, representative here for the tunnel width and wall thickness. The GRF synthesized structures are built of superposed waves of only one wavelength, which is representative for only one average pore size and wall width, responsible for rather prominent local minima and maxima.

Static and dynamic invariant extraction. Common features which do not change irrespective of any smooth coordinate transformations[41] applied are called statistical or dynamic invariant,[43] and can be used to compare the complexity of various structures by just calculating a scalar value. To obtain this scalar, structural properties are averaged globally over the sample data series. The correlation dimension (as a static invariant) was already used by Dathe et al.[83] to characterize porous structures. Nauer et al. applied the correlation dimension to measure the complexity of termite mound surfaces.[13] The permutation entropy H and statistical complexity C (as part of the class of dynamic invariant measures) were, for example, used by Sigaki et al.[84] as a feature for a machine learning application to predict physical properties of liquid crystals.

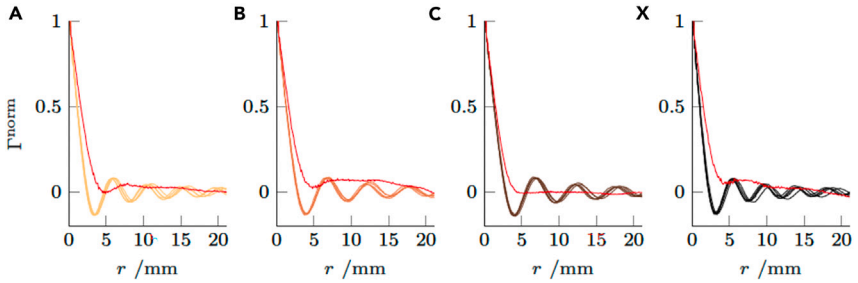

Figure 13. Normalized two-point autocorrelation functions

Γ^{norm} for filtered μCT scans (red lines) and their respective GRFs for samples A, B, C, and X.

Correlation dimension. Similar to the box counting dimension, the correlation dimension D_2 (a static invariant) captures the structure's complexity.[41] Because the structure is defined by the three-dimensional interface between volume and pores, D_2 can take values between 2 (surface-covering) and 3 (volume-filling).[41,85] A higher non-integer value indicates a more complex topological composition on different scales. Here the correlation dimension is computed for the binarized volumes of the filtered μCT scans and the GRFs.[41]

The correlation integral is the average number of points of a domain inside a sphere with radius r:

$$C(r) = \lim_{N\to\infty} \frac{1}{N^2} \sum_{i,j=1}^{N} \Theta\left(r - \left|\mathbf{x}_i - \mathbf{x}_j\right|\right) \quad \text{(Equation 6)}$$

where Θ is the Heaviside function. The correlation dimension $D = D_2$[80] is defined as the exponent of the increase of the correlation integral C with the radius r[85]:

$$C(r) \propto r^D, \quad \text{(Equation 7)}$$

thus $D = \log(C(r))/\log(r) = D_2$.

Permutation entropy. Entropy (a dynamic invariant) as such is a measure which also relates to a structure's complexity.[86,87] The entropy, as a measure of information generation (or expected uncertainty) in the data,[88] is converges over a range of scales the more permutations are needed to sort the structure into a regular pattern; generally speaking for periodic processes, the entropy converges to zero, and for random processes it becomes larger and diverges for all scales (infinite for infinitely large datasets), while a deterministic chaotic process converge to a plateau of a finite, non-zero value at intermediate length scales.[41] The permutation entropy H is the normalized version of the Shannon entropy S of the probability distribution P of all local permutations of elements within the structure. It can be defined as[84]

$$H(P) = \frac{1}{\ln(n)} \sum_{i=0}^{n} p_i \ln\left(1 / p_i\right) = \frac{1}{\ln(n)} S(P) \quad \text{(Equation 8)}$$

The probability distribution P is calculated according to[84] by counting the incidence of individual permutation operators which sort the elements within a sliding window.

Statistical complexity. The statistical complexity C norms the permutation entropy with the Jensen-Shannon divergence to account for high-dimensionality and is derived from the permutation entropy and defined as[84,89]

$$C(P) = \frac{Q(P,U)H(P)}{Q_{max}} \quad \text{(Equation 9)}$$

where Q is is the Jensen-Shannon divergence between P and the uniform distribution U, and Q_{max} is the theoretical maximum of Q.[89] Purely random and perfectly ordered structures have a complexity of $C = 0$. Values for the entropy and the statistical complexity are estimated using a sliding window (a moving subcube) of 2×3×1 voxels averaged in each direction with 6! = 720 permutations. This number of permutations is smaller than using the default window for the sliding cube of 2×2×2 which has 40,320 possible permutations, and decreases the ratio of subcube to full cube permutations (128!) hence reduces the likelihood of drawing identical permutations by chance (see also example in Appendix of Sikaki et al. (2019)[84]).

Surface to volume ratio. The surface to volume ratio is defined as A/V_{tot}. The total volume is given by the volume of a cube $V_{tot} = a^3$, where a is the length of one edge. The surface area A for the samples is determined numerically by generating a mesh of the internal surface (excluding the planar cut surfaces) and summing up the areas of every triangular surface element.

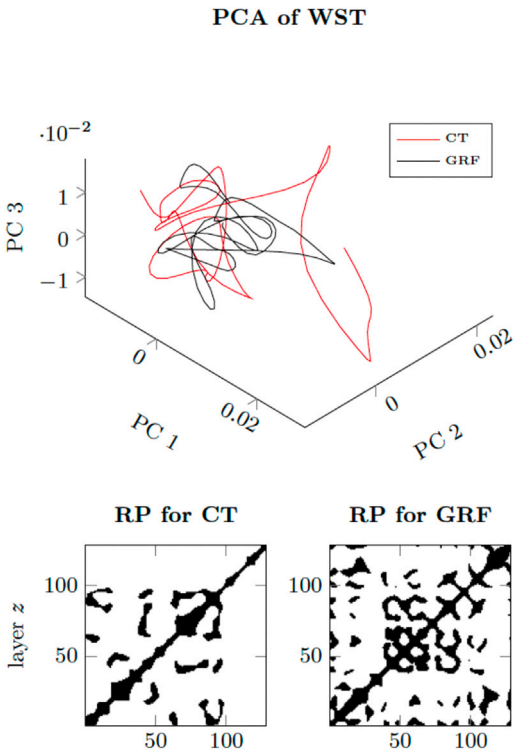

Figure 14. Feature space trajectory and Recurrence plot

FST and RP for the μT scan and a GRF of sample X. The PCA is calculated independently for each sample, resulting in different coordinates for the FST. The recurrence plot for the GRF shows a much more regular structure than for the μCT scan.

Graphs. The Euler characteristic for graphs can be defined as[60]

$$\chi = N_n - N_b \quad \text{(Equation 10)}$$

where N_n is the number of nodes and N_b is the number of bonds. This quantity is independent of the degree of simplification of the network, because adding a node to existing branches increases N_n and N_b by one, each.

Recurrence plots. Recurrence plots were introduced by Eckmann et al. (1987).[90] They are a visual representation of the recurrence matrix $\mathbf{R}$, which is a thresholded similarity matrix of the states $\mathbf{x}$ in the phase space. Recurrence plots (RP) can be used to characterize nonlinear dynamical systems or stochastic processes[34,44] which is also expandable to spatial analyzes.[34,44]

The recurrence matrix is generally defined as[34]

$$R_{i,j}(\varepsilon) = \Theta\left(\varepsilon - \left|\mathbf{x}_i - \mathbf{x}_j\right|\right), i, j = 1, \ldots, N \quad \text{(Equation 11)}$$

where Θ is the Heaviside function, ε is the threshold for the epsilon environment and $\mathbf{x} \in \mathbb{R}^m$ is the m-dimensional trajectory in phase space of length N. To set up the state space usually embedding techniques are used; in particular, the so-called Takens delay embedding with an embedding delay τ and an embedding dimension m (more detail[34,43]).

For this study $\mathbf{x}$ is a state of the wavelet scattering transform feature space trajectory after reducing the dimensionality of the feature space using a PCA. Here not the delay embedding but the first three components of the PCA have been used which also contains most of the information. The recurrence plots are generated using the CRP toolbox by Marwan et al. (2007),[34] using a fixed threshold of $\varepsilon = 0.0075$ with Euclidean distance as threshold criterion. The recurrence quantification analysis (RQA) measures are computed for the full RP of each sample. The Theiler window is set to $t_w = 6$.

Figure 14 shows the FSTs for the μCT scan and an optimized GRF of sample X. Other than for Figure 5 the PCA for each sample is calculated independently of the other samples, because for this analysis we are interested in the differences within each sample, not between the samples. Hence, each sample has individual coordinate axes. Their trajectories however can be compared qualitatively.

Limitations of the study

Computed tomography scans used in here are expensive, as specialist equipment and analyses are required. Hence, the number of specimens studied is limited to cost and effort of collection, sample preparation, and scanning involved.

It would be interesting to have a range of different structures within one nest and across species studied to better understand their functional topology.

STAR★METHODS

Detailed methods are provided in the online version of this paper and include the following:

- KEY RESOURCES TABLE
- RESOURCE AVAILABILITY
  - Lead contact
  - Materials availability
  - Data and code availability
- EXPERIMENTAL MODEL AND STUDY PARTICIPANT DETAILS
- METHOD DETAILS

ACKNOWLEDGMENTS

The authors would like to thank Travers Sansom and Alison Böni, who helped in preparation and execution of the required field work, as well as processing of samples at the University of New South Wales Canberra campus. Prof Joseph Lai and Dr Merten Stender provided some feedback on the first draft of the manuscript. Further the authors wish to thank A/Prof. Mohammad Saadatfar of the Australian National University for providing the μCT-Scans. The authors acknowledge a license for scientific activities under the Nature Conservation Act 2014 within the ACT Tidbinbilla Nature Reserve (license TS20188 held by S.O.). This research was supported under Australian Research Councils (ARC) Discovery Projects funding scheme project no. DP200100358) and was further supported through a UTS FEIT Blue Sky grant (2018).

AUTHOR CONTRIBUTIONS

Author contributions have been evaluated according to CRediT: S.O. – conceptualization, methodology, validation, investigation, formal analysis, resources, data curation, writing the original draft, revising and editing the manuscript, visualization, project administration, and funding acquisition. R.M. – conceptualization, methodology, software, validation, formal analysis, investigation, resources, data curation, writing the original draft, documentation and materials, revising and editing the manuscript, and visualization.

DECLARATION OF INTERESTS

The authors declare that they have no competing interests. S.O. has an additional affiliation at the Hamburg University of Technology as visiting fellow, which is unrelated to the work presented in this paper. R.M. has his current affiliation at the CAPS Laboratory, Mechanical and Process Engineering Department, ETH Zürich, Switzerland where he conducts research as PhD candidate. The work of the manuscript is unrelated to the current affiliation.

INCLUSION AND DIVERSITY

We support inclusive, diverse, and equitable conduct of research.

Received: January 27, 2023
Revised: July 9, 2023
Accepted: December 5, 2023
Published: December 14, 2023

REFERENCES

1. Seeley, T.D. (1989). The honey bee colony as a superorganism. Am. Sci. *77*, 546–553.
2. Camazine, S., Deneubourg, J., Franks, N.R., Sneyd, J., Bonabeau, E., and Theraulaz, G. (2001). Self-organization in Biological Systems (Princeton University).
3. Perna, A., and Theraulaz, G. (2017). When social behaviour is moulded in clay: on growth and form of social insect nests. J. Exp. Biol. *220*, 83–91.
4. Turner, J.S. (2004). The Extended Organism. The Physiology of Animal-Built Structures (Harvard University Press), p. 235.
5. Chiri, E., Nauer, P.A., Lappan, R., Jirapanjawat, T., Waite, D.W., Handley, K.M., Hugenholtz, P., Cook, P.L.M., Arndt, S.K., and Greening, C. (2021). Termite gas emissions select for hydrogenotrophic microbial communities in termite mounds. Proc. Natl. Acad. Sci. USA *118*, e2102625118.
6. Santamaría, C., Armbrecht, I., and Lachaud, J.-P. (2022). Nest architecture and colony composition in two populations of *Ectatomma ruidum* sp. 2 (*E. ruidum* species complex) in southwestern colombia. PLoS One *17*, e0263382.
7. Oberst, S., Lai, J.C.S., Martin, R., Halkon, B.J., Saadatfar, M., and Evans, T.A. (2020). Revisiting stigmergy in light of multi-functional, biogenic, termite structures as communication channel. Comput. Struct. Biotechnol. J. *18*, 2522–2534.
8. Korb, J. (2010). Termite Mound Architecture, from Function to Construction. In Biology of Termites: a Modern Synthesis, D.E. Bignell, Y. Roisin, and N. Lo, eds. (Springer Netherlands), pp. 349–373.
9. Singh, K., Muljadi, B.P., Raeini, A.Q., Jost, C., Vandeginste, V., Blunt, M.J., Theraulaz, G., and Degond, P. (2019). The architectural design of smart ventilation and drainage systems in termite nests. Sci. Adv. *5*, eaat8520.
10. Krishna, K., Grimaldi, D., and Engel, M. (2013). Treatise on the isoptera of the world: vol. 1. Bull. Am. Mus. Nat. Hist. *377*, 1–196.
11. Beasley-Hall, P.G., Chui, J., Arab, D.A., and Lo, N. (2018). Evidence for a complex evolutionary history of mound building in the Australian nasute termites (Nasutitermitinae). Biol. J. Linn. Soc. Lond. *126*, 304–314.
12. Oberst, S., Martin, R., Halkon, B.J., Lai, J.C.S., Evans, T.A., and Saadatfar, M. (2021). Submillimetre mechanistic designs of termite-built structures. J. R. Soc. Interface *18*.
13. Nauer, P.A., Chiri, E., de Souza, D., Hutley, L.B., and Arndt, S.K. (2018). Technical note: Rapid image-based field methods improve the quantification of termite mound

structures and greenhouse-gas fluxes. Biogeosciences *15*, 3731–3742.
14. Perna, A., Jost, C., Couturier, E., Valverde, S., Douady, S., and Theraulaz, G. (2008). The structure of gallery networks in the nests of termite Cubitermes spp. revealed by X-ray tomography. Naturwissenschaften *95*, 877–884.
15. Perna, A., Valverde, S., Gautrais, J., Jost, C., Solé, R., Kuntz, P., and Theraulaz, G. (2008). Topological efficiency in three-dimensional gallery networks of termite nests. Phys. Stat. Mech. Appl. *387*, 6235–6244.
16. Facchini, G., Lazarescu, A., Perna, A., and Douady, S. (2020). A growth model driven by curvature reproduces geometric features of arboreal termite nests. J. R. Soc. Interface *17*, 20200093.
17. Theraulaz, G., and Bonabeau, E. (1999). A brief history of stigmergy. Artif. Life *5*, 97–116.
18. Heyde, A., Guo, L., Jost, C., Theraulaz, G., and Mahadevan, L. (2021). Self-organized biotectonics of termite nests. Proc. Natl. Acad. Sci. USA *118*, e2006985118.
19. Bonabeau, E. (1999). Editor's introduction: Stigmergy. Artif. Life *5*, 95–96.
20. Calovi, D.S., Bardunias, P., Carey, N., Scott Turner, J., Nagpal, R., and Werfel, J. (2019). Surface curvature guides early construction activity in mound-building termites. Philos. Trans. R. Soc. Lond. B Biol. Sci. *374*, 20180374.
21. Sim, S., Kang, S.-H., and Lee, S.-H. (2015). Using hidden Markov models to characterize termite traveling behavior in tunnels with different curvatures. Behav. Process. *111*, 101–108.
22. Lee, S.-H. (2017). Effects of tunnel slopes on movement efficiency and behavior of termites. Orient. Insects *51*, 370–379.
23. Facchini, G., Rathery, A., Douady, S., Sillam-Dussès, D., and Perna, A. (2023). Substrate evaporation drives collective construction in termites. Elife *12*, RP86843.
24. Himmi, S.K., Yoshimura, T., Yanase, Y., Oya, M., Torigoe, T., and Imazu, S. (2014). X-ray tomographic analysis of the initial structure of the royal chamber and the nest-founding behavior of the drywood termite Incisitermes minor. J. Wood Sci. *60*, 453–460.
25. Berville, L., and Darrouzet, E. (2019). Wood excavation, construction, and architecture in two reticulitermes subterranean termites. Insectes Soc. *66*, 403–411.
26. Ku, S.J., Su, N.-Y., and Lee, S.-H. (2013). Movement Efficiency and Behavior of Termites (Isoptera) in Tunnels with Varying Pore Sizes. Fla. Entomol. *96*, 810–817.
27. Lee, S.-B., Su, N.-Y., Song, H.-S., and Lee, S.-H. (2020). Minimizing moving distance in deposition behavior of the subterranean termite. Ecol. Evol. *10*, 2145–2152.
28. Gomez, L., Alvarez, L., Mazorra, L., and Frery, A.C. (2017). Fully PolSAR image classification using machine learning techniques and reaction-diffusion systems. Neurocomputing *255*, 52–60. Bioinspired Intelligence for machine learning.
29. Yasuda, H., Yamaguchi, K., Miyazawa, Y., Wiebe, R., Raney, J.R., and Yang, J. (2020). Data-driven prediction and analysis of chaotic origami dynamics. Commun. Phys. *168*.
30. Liu, Y., Li, J., Sun, S., and Yu, B. (2019). Advances in Gaussian random field generation: a review. Comput. Geosci. *23*, 1011–1047.
31. Kennedy, D.P. (1994). The term structure of interest rates as a Gaussian random field. Math. Finance *4*, 247–258.
32. Mallat, S.G. (2009). A Wavelet Tour of Signal Processing: The Sparse Way, 3rd edition (Elsevier/Academic Press).
33. Mallat, S. (2012). Group Invariant Scattering. Commun. Pure Appl. Math. *65*, 1331–1398.
34. Marwan, N., Carmen Romano, M., Thiel, M., and Kurths, J. (2007). Recurrence plots for the analysis of complex systems. Phys. Rep. *438*, 237–329.
35. Limaye, A. (2012). Drishti: A Volume Exploration and Presentation Tool.
36. Oberst, S., Baro, E.N., Lai, J.C.S., and Evans, T.A. (2014). Quantifying ants' activity using vibration measurements. PLoS One *9*, 90902.
37. Regis, R.G., and Shoemaker, C.A. (2007). A stochastic radial basis function method for the global optimization of expensive functions. Inf. J. Comput. *19*, 497–509.
38. Taud, H., Martinez-Angeles, R., Parrot, J.F., and Hernandez-Escobedo, L. (2005). Porosity estimation method by X-ray computed tomography. J. Pet. Sci. Eng. *47*, 209–217.
39. Kumar, S., Tan, S., Zheng, L., and Kochmann, D.M. (2020). Inverse-designed spinodoid metamaterials. npj Comput. Mater. *6*, 73.
40. Spanos, A. (1999). Probability Theory and Statistical Inference (Cambridge University Press).
41. Kantz, H., and Schreiber, T. (2004). Nonlinear Time Series Analysis (Cambridge University Press).
42. Baccetti, V., and Visser, M. (2013). Infinite Shannon entropy. J. Stat. Mech. *2013*, P04010.
43. Oberst, S., and Lai, J.C.S. (2015). A statistical approach to estimate the Lyapunov spectrum in disc brake squeal. J. Sound Vib. *334*, 120–135.
44. Marwan, N., Kurths, J., and Saparin, P. (2007). Generalised recurrence plot analysis for spatial data. Phys. Lett. *360*, 545–551.
45. Oberst, S., and Martin, R. (2023). Additional Data: Feature-Preserving Synthesis of Termite-Mimetic Spinodal Nest Morphology (Zenodo).
46. Puri, S., and Oono, Y. (1988). Effect of noise on spinodal decomposition. J. Phys. Math. Gen. *21*, L755–L762.
47. Bardunias, P.M., Calovi, D.S., Carey, N., Soar, R., Turner, J.S., Nagpal, R., and Werfel, J. (2020). The extension of internal humidity levels beyond the soil surface facilitates mound expansion in *Macrotermes*. Proc. Biol. Sci. *287*, 20200894.
48. Oberst, S., Lai, J.C.S., and Evans, T.A. (2016). Termites utilise clay to build structural supports and so increase foraging resources. Sci. Rep. *6*, 20990.
49. Zachariah, N., Das, A., Murthy, T.G., and Borges, R.M. (2017). Building mud castles: a perspective from brick-laying termites. Sci. Rep. *7*, 4692.
50. Zachariah, N., Singh, S., Murthy, T.G., and Borges, R.M. (2020). Bi-layered architecture facilitates high strength and ventilation in nest mounds of fungus-farming termites. Sci. Rep. *10*, 13157.
51. Jouquet, P., Harit, A., Cheik, S., Traoré, S., and Bottinelli, N. (2019). Termites: Soil engineers for ecological engineering. Comptes Rendus Biol. *342*, 258–259. Insects: Friends, foes, and models/Insectes : amis, ennemis et modèles.
52. Cheik, S., Jouquet, P., Maeght, J., Capowiez, Y., Tran, T., and Bottinelli, N. (2021). X-ray tomography analysis of soil biopores structure under wetting and drying cycles. Soil Sci. *72*, 2128–2132.
53. Jiang, Z., Chen, W., and Burkhart, C. (2013). efficient 3D porous microstructure reconstruction via Gaussian random field and hybrid optimization. J. Microsc. *252*, 135–148.
54. Kandasami, R.K., Borges, R.M., and Murthy, T.G. (2016). Effect of biocementation on the strength and stability of termite mounds. Environmental Geotechnics *3*, 99–113.
55. Zappalorto, M., Salviato, M., Pontefisso, A., and Quaresimin, M. (2013). Notch effect in clay-modified epoxy: a new perspective on nanocomposite properties. Compos. Interfac. *20*, 405–419.
56. Hu, K., Lu, C., Yu, B., Yang, L., and Rao, Y. (2023). Optimization of bionic heat sinks with self-organized structures inspired by termite nest morphologies. Int. J. Heat Mass Tran. *202*, 123735.
57. Xiong, Q., Baychev, T.G., and Jivkov, A.P. (2016). Review of pore network modelling of porous media: Experimental characterisations, network constructions and applications to reactive transport. J. Contam. Hydrol. *192*, 101–117.
58. J.J. Skrzypek, and A.W. Ganczarski, eds. (2015). Mechanics of Anisotropic Materials (Springer Cham).
59. Testa, B., and Kier, L. (2000). Emergence and dissolvence in the self-organisation of complex systems. Entropy *2*, 1–25.
60. Vogel, H.-J. (2002). Topological Characterization of Porous Media. In Morphology of Condensed Matter, *volume 600*, R. Beig, B.-G. Englert, U. Frisch, P. Hänggi, K. Hepp, W. Hillebrandt, D. Imboden, R.L. Jaffe, R. Lipowsky, and v. Löhneysen, et al., eds. (Springer Berlin Heidelberg), pp. 75–92.
61. Esteban, L., Géraud, Y., and Bouchez, J.L. (2007). Pore network connectivity anisotropy in Jurassic argillite specimens from eastern Paris Basin (France). Phys. Chem. Earth *32*, 161–169.
62. King, P., and Masihi, M. (2021). Percolation in Porous Media (Complex Media Percolation Theory), pp. 237–254.
63. Masihi, M., Shams, R., and King, P.R. (2022). Pore level characterization of micro-CT images using percolation theory. J. Pet. Sci. Eng. *211*, 110113.
64. Momeni Pakdehi, D., Aprojanz, J., Sinterhauf, A., Pierz, K., Kruskopf, M., Willke, P., Baringhaus, J., Stöckmann, J.P., Traeger, G.A., Hohls, F., et al. (2018). Minimum resistance anisotropy of epitaxial graphene on sic. ACS Appl. Mater. Interfaces *10*, 6039–6045.
65. Dong, S., Xia, Y., Huang, R., and Zhao, J. (2020). Modulating mechanical anisotropy of two-dimensional materials by controlling their defects. Carbon *158*, 77–88.
66. Ireland, T., and Garnier, S. (2018). Architecture, space and information in constructions built by humans and social insects: a conceptual review. Phil. Trans. R. Soc. *373*, 20170244.
67. Turner, J.S. (2011). Termites as models of swarm cognition. Swarm Intell. *5*, 19–43.
68. Melnikov, A., Chiang, Y.K., Quan, L., Oberst, S., Alù, A., Marburg, S., and Powell, D. (2019). Acoustic meta-atom with experimentally verified maximum Willis coupling. Nat. Commun. *10*, 3148.
69. Hadlington, S., and Staunton, I. (2008). Australian Termites, 3rd ed. (University of New South Wales Press Ltd).
70. Jawerth, B., and Sweldens, W. (1994). An overview of wavelet based multiresolution analyses. SIAM Rev. *36*, 377–412.

71. Pastor, L., Rodríguez, A., Espadero, J., and Rincón, L. (2001). 3d wavelet-based multiresolution object representation. Pattern Recogn. *34*, 2497–2513.
72. Ocko, S.A., Heyde, A., and Mahadevan, L. (2019). Morphogenesis of termite mounds. Proc. Natl. Acad. Sci. USA *116*, 3379–3384.
73. Sheppard, A.P., Sok, R.M., and Averdunk, H. (2004). Techniques for image enhancement and segmentation of tomographic images of porous materials. Phys. Stat. Mech. Appl. *339*, 145–151. Proceedings of the International Conference New Materials and Complexity.
74. Sheppard, A., Latham, S., Middleton, J., Kingston, A., Myers, G., Varslot, T., Fogden, A., Sawkins, T., Cruikshank, R., Saadatfar, M., et al. (2014). Techniques in helical scanning, dynamic imaging and image segmentation for improved quantitative analysis with X-ray micro-CT. Nucl. Instrum. Methods Phys. Res. Sect. B Beam Interact. Mater. Atoms *324*, 49–56. 1st International Conference on Tomography of Materials and Structures.
75. Bruna, J., and Mallat, S. (2013). Invariant Scattering Convolution Networks. IEEE Trans. Pattern Anal. Mach. Intell. *35*, 1872–1886.
76. Andén, J., and Mallat, S. (2014). Deep scattering spectrum. IEEE Trans. Signal Process. *62*, 4114–4128.
77. Soyarslan, C., Bargmann, S., Pradas, M., and Weissmüller, J. (2018). 3D stochastic bicontinuous microstructures: Generation, topology and elasticity. Acta Mater. *149*, 326–340.
78. Adler, R.J., and Taylor, J.E. (2011). Random Fields and Geometry (Springer-Verlag).
79. dos Santos, M.A. (2019). Analytic approaches of the anomalous diffusion: A review. Chaos, Solit. Fractals *124*, 86–96.
80. Oberst, S., Niven, R.K., Lester, D.R., Ord, A., Hobbs, B., and Hoffmann, N. (2018). Detection of unstable periodic orbits in mineralising geological systems. Chaos *28*, 085711.
81. Cahn, J.W. (1965). Phase Separation by Spinodal Decomposition in Isotropic Systems. J. Chem. Phys. *42*, 93–99.
82. Jordaan, J., Punzet, S., Melnikov, A., Sanches, A., Oberst, S., Marburg, S., and Powell, D.A. (2018). Measuring monopole and dipole polarisability of acoustic meta-atoms. Appl. Phys. Lett. *113*, 224102.
83. Dathe, A., Tarquis, A.M., and Perrier, E. (2006). Multifractal analysis of the pore- and solid-phases in binary two-dimensional images of natural porous structures. Geoderma *134*, 318–326.
84. Sigaki, H.Y.D., de Souza, R.F., de Souza, R.T., Zola, R.S., and Ribeiro, H.V. (2019). Estimating physical properties from liquid crystal textures via machine learning and complexity-entropy methods. Phys. Rev. E *99*, 013311.
85. Grassberger, P. (1983). Generalized dimensions of strange attractors. Phys. Lett. *97*, 227–230.
86. Lu, S., Oberst, S., Zhang, G., and Luo, Z. (2019). Novel Order Patterns Recurrence Plot-Based Quantification Measures to Unveil Deterministic Dynamics from Stochastic Processes (Switzerland: Springer Cham), pp. 57–70.
87. Amigó, J.M., Dale, R., and Tempesta, P. (2021). A generalized permutation entropy for noisy dynamics and random processes. Chaos *31*, 013115.
88. Oberst, S., and Lai, J.C.S. (2011). Chaos in brake squeal noise. J. Sound Vib. *330*, 955–975.
89. Ribeiro, H.V., Zunino, L., Lenzi, E.K., Santoro, P.A., and Mendes, R.S. (2012). Complexity-Entropy Causality Plane as a Complexity Measure for Two-Dimensional Patterns. PLoS One *7*, e40689.
90. Eckmann, J.-P., Kamphorst, S.O., and Ruelle, D. (1987). Recurrence Plots of Dynamical Systems. Europhys. Lett. *4*, 973–977.

STAR★METHODS

KEY RESOURCES TABLE

REAGENT or RESOURCE	SOURCE	IDENTIFIER
Biological samples		
Termite mound materials of (1) *Nasutitermes exitiosus* (Hill) and (2) *Coptotermes lacteus* (Froggatt)	(1) Collection location: Near the Australian Defence Force Academy in Canberra, ACT, Australia (35.30 deg S, 149.17 deg E) (2) Tidbinbilla Nature Reserve, ACT, Australia (35.456 deg S, 148.927 deg E);	NA
Deposited data		
Raw and analyzed data	This paper and in depositories	File repository Zenodo[45] https://doi.org/10.5281/zenodo.7421410 Additional data of *N. exitiosus* has been used here and is linked to previous study[12]
Software and algorithms		
MATLAB R2021a in particular functions (1) **pca.m** (Principal component analysis) (2) **permEntr.m** (Permutation entropy) (3) **waveletScattering2.m** (2D wavelet scattering for images)	The MathWorks, Inc., Natick, MA, US	Matlab, RRID:SCR_001622, manuals, online
CT software *Drishti v3.1	Ajay Limaye (2012)[35]	Drishti, RRID:SCR_017999, Github, file depository
Instrumentation/facility *Mango: Australian National University (ANU) Medial Axis and Network Generation software	Sheppard et al. (2014)[74]	Instrumentation used website
Graphics * EazyDraw 10.5.3	EazyDraw, a Dekorra Optics LLC enterprise	EazyDraw, RRID:SCR_024814, website
Text processing * Overleaf and * TexShop 5.12	Overleaf c/o Digital Science (London) TeXShop is distributed under the GPL public license, and thus free.	Overleaf, RRID:SCR_003232, website TechShop website
Other packages which can be used/ have been used/ could be useful in course of this study	(1) Marwan's Cross recurrence toolbox TOCSY (2) Hegger et al.s TISEAN package (3) TS toolbox -	(1) TOCSY website (2) TISEAN website (3) TS toolbox website

RESOURCE AVAILABILITY

Lead contact

Further information and requests for resources should be directed to and will be fulfilled by the lead contact, Sebastian Oberst (sebastian.oberst@uts.edu.au).

Materials availability

This study did not generate new unique reagents.

Data and code availability

- Micro-CT data have been deposited at *Zenodo* and are publicly available as of the date of publication. Accession numbers are listed in the key resources table and reference list.
- This paper did not generate original code. Matlab scripts using publicly available functions and scripts can be downloaded from the Zenodo file depository provided in the key resources table.
- Any additional information required to reanalyse the data reported in this paper is available from the lead contact upon request.

EXPERIMENTAL MODEL AND STUDY PARTICIPANT DETAILS

Termite nest specimens were collected in Canberra, Australian Capital Territory (see key resources table for coordinates).

METHOD DETAILS

All method details have been provided within the manuscript. Any additional information required to reanalyse the data reported in this paper is available from the lead contact upon request.